Structural, Electronic and Transport Properties of Hybrid $SrTiO_3$-Graphene and Carbon Nanoribbon Interfaces

J. D. Baran[1,*], C. Eames[1], K. Takahashi[2,3], M. Molinari[1,4], M. Saiful Islam[1] and S.C. Parker[1,*]

[1]*Department of Chemistry, University of Bath, Claverton Down, Bath BA2 7AY, UK*
[2]*Center for Materials Research by Information Integration (CMI2), National Institute for Materials Science (NIMS), 1-2-1 Sengen, Tsukuba, Ibaraki 305-0047, Japan*
[3]*Graduate School of Engineering, Hokkaido University, N-13, W-8, Sapporo 060-8628, Japan*
[4]*Department of Chemistry, University of Huddersfield, Huddersfield, HD1 3DH, U.K.*

*Corresponding authors: S.C.Parker@bath.ac.uk

Abstract

Hybrid materials composed of different functional structural units offer the possibility of tuning both the thermal and electronic properties of a material independently. Using quantum mechanical calculations, we investigate the change in the electronic and thermoelectric transport properties of graphene and hydrogen-terminated carbon nanoribbons (CNRs) when these are placed on the SrTiO3 (001) surface (STO). We predict that both p-type and n-type composite materials can be achieved by coupling graphene/CNR to different surface terminations of STO. We show that the electronic properties of graphene and CNR are significantly altered on SrO-terminated STO but are preserved upon interaction with TiO2-terminated STO and that CNRs possess distinct electronic states around the Fermi level because of their quasi-one-dimensional nature, leading to a calculated Seebeck coefficient much higher than that of a pristine graphene sheet. Moreover, our calculations reveal that in the TiO2-SrTiO3/CNR system there is a favorable electronic level alignment between the CNR and STO, where the highest occupied molecular orbital of the CNR is positioned in the middle of the STO band gap, resembling n-type doping of the substrate. Our results offer design principles for guiding the engineering of future hybrid thermoelectric materials and, more generally, nanoelectronic materials comprising oxide and graphitic components.

Introduction

Many approaches to improve the thermoelectric properties of materials have been tried. Among these are doping,1 nano-engineering,2,3 and dimensionality reduction.4 However, despite extensive research for decades, applications of thermo-electric devices composed of earth abundant and nontoxic materials are still limited. The figure of merit for a thermoelectric material is ZT = S2σT/(ke + kl), with S the Seebeck coefficient, σ being the electronic conductivity, T being the temperature, and ke and kl being the thermal electronic and phonon conductivity, respectively. High values of ZT are difficult to obtain because the component variables are very difficult to control independently. This originates from the fact that all but kl are related to the electronic structure of a material and are therefore interdependent. For example, increasing the Seebeck coefficient decreases the electronic conductivity and vice versa.2 Previous improvements in ZT have been due to selecting materials on the basis of careful consideration of their electronic and thermal properties and are mostly related to bulk three-dimensional cases. The next logical step is to make materials modular, where each module plays a distinct role. Such hybrid materials can be considered combinations of building blocks with different electrical and thermal properties. Thus, by selectively choosing individual components, with distinct electronic and thermal properties, one could in principle achieve a material with desired properties that are not exhibited by any of the bulk components.5 Two-dimensional multilayer systems are the simplest example of hybrid materials and so far have not been investigated to the same extent as the bulk materials. These thin film systems are increasingly important because of the constant miniaturization of electronic components and advances in nanoscale fabrication that enable tailoring of their properties.6

The physics and chemistry at the interface between different material components dominate the electronic properties of the overall system. At the atomic scale, the interaction between different parts of a hybrid material involves bond rehybridiza-tion and charge transfer, which modifies the electronic transport properties, e.g., electronic conductivity or Seebeck coefficient. In addition, modular design enhances phonon scattering, which results in a reduced thermal conductivity.2 The fundamental challenge for hybrid thermoelectrics and nanoelectronic materials is to find the composite materials that result in the desired efficiency and properties of the overall device. To address this challenge, an effective strategy is required to identify suitable modular components.

One such class of modular materials consists of oxides, whose electronic structure is well understood and can be readily controlled. $SrTiO_3$ has a large carrier effective mass resulting in a high Seebeck coefficient, good thermal stability at high temperature, and strong structural tolerance for substitutional doping.1 However, its application as a thermoelectric material is currently limited by a high operating temperature of >700 °C.7 Other

modular materials that are particularly interesting from a fundamental point of view and because of their technological relevance are graphene and its derivatives. It has recently been shown that the thermal operating window of STO can be cooled to room temperature by the addition of graphene nanoflakes during preparation.8 The unusual band structure of graphene gives rise to a variety of intriguing electrical and thermal phenomena.9 Among them are remarkable electronic transport properties, such as a record carrier mobility of ∼2 × 105 cm2 V−1 s−1 and a Seebeck coefficient (S) of ∼80 μV K−1.10,11 However, because of its extremely high thermal conductivity (k) of 2−5 × 103 W/m,12−14 its overall ZT at a room temperature of ∼0.0110−12 is at least 2 orders of magnitude below that of leading thermoelectric materials.2

Despite the extremely high thermal conductivity of graphene, it has been shown that addition of graphene nanoflakes to the STO decreases the thermal conductivity of STO.8 Because of the system size (see Methodology), first-principles calculations of the lattice thermal conductivity are computationally prohibitive for us at present. However, it has been recently shown that introduction of patterns on the graphene by its functionalization decreases thermal conductivity while keeping the power factor and electronic conductivity high, resulting in a predicted ZT of 3 at room temperature.15 Chen et al.16 showed that in case of the graphene/h-BN interface the overall superlattice thermal conductivity was decreased by 83% when compared with those of the parent materials, which indicates that construction of superlattice structures may be an efficient method of decreasing the lattice thermal conductivity of graphene. The work of Yeandel et al.17 showed that by nanostructuring $SrTiO_3$ a lower thermal conductivity over a broad range of temperatures can be achieved. Even more interesting electronic properties can be found in elongated strips of graphene with a finite width such as carbon nanoribbons (CNRs). CNRs can be either metallic or semiconducting depending on the crystallographic direction of the ribbon axis and may present unique magnetic properties.18 Moreover, because of technical advances, they can be produced in a highly controllable manner, which opens up great opportunities for the future design of such hybrid nanomaterials.19−22

Here, we will focus on the structural, electronic, and thermoelectric transport properties of pristine graphene and CNR and their interfaces with the STO surface. We will discuss the nature of interactions at the STO/graphene (CNR) interface and how this affects the electronic and transport properties of the composite system. First, we outline the computational methodology, and then we report the structural and electronic properties of interfaces of graphene and CNR with TiO_2- and SrO-terminated (001) $SrTiO_3$ (STO) surfaces. Finally, we discuss the thermoelectric transport properties of these interfaces and compare them to the properties of the free graphene sheet and CNR.

Methodology

Interface Design. For STO bulk, pristine graphene, and CNR, the Monkhorst−Pack k-meshes used were 8 × 8 × 8, 14 × 14 × 1, and 4 × 14 × 1, respectively. In the case of the single layer of graphene and CNR, a thick vacuum layer of 20 Å was used and a dipole correction along the surface normal was applied. The electronic convergence was 1 × 10−8 eV, and the force on each atom was optimized to <1 × 10−3 eV/Å. These settings result in calculated lattice constants of 3.949 and 2.460 Å for STO bulk and graphene, respectively, in good agreement with previous studies.23 Here we use hydrogen-terminated zigzag CNR, with a width of 3 and a length of 1 unit cell (see Figure 1d). The choice of the zigzag CNR was dictated by its excellent epitaxial match to the STO surface as discussed below.

To model the interfaces, the lattice vectors of the STO and graphene/CNR were redefined as shown in Figure 1a−d to find the best compromise between system sizes and mean absolute strain between the two components. For the STO/graphene interface, the graphene sheet is strained by 0.42% along the ε'11 vector and 0.35% along the ε'22 vector (Figure 1b) and then matched with the ε11 and ε22 unit cell vectors of the STO surface, which results in a mean absolute strain of 0.90%. Similarly, in the case of the STO/CNR interface, the CNR of 8 × 3 periodicity has been matched to the 3 × 5 STO surface (Figure 1c,d), which resulted in stretching the CNR by 0.35% along ϕ'11. We performed a potential energy surface scan to determine the lateral position of the CNR on STO. The scan was performed with steps of 0.05ϕ11 and 0.01ϕ22, which resulted in 36 different configurations. All atoms were fully relaxed in this process. The $SrTiO_3$ (001) surfaces consist of alternating TiO_2 and SrO (001) layers and thereby can have two possible terminations, either TiO_2-terminated (hereafter termed Ti-STO) or SrO-terminated (hereafter termed Sr-STO).24 In this work, an 11-molecular layers thick slab of STO was used, and both nonstoichiometric surfaces with TiO_2/TiO_2 and SrO/SrO termination at both ends as well as stoichiometric with TiO_2/SrO terminations were considered. However, because of difficulties in the separation of electronic contributions from the TiO_2- and SrO-terminated surface within the same slab for the stoichiometric compositions, we will consider only the nonstoichiometric terminations here. A vacuum layer of 20 Å and a dipole correction along the surface normal were applied.

Geometry Optimization. The ground state atomic and electronic structure was calculated with first-principles density functional theory, using the plane-wave DFT code VASP.25−27 Core electrons were represented by PAW pseudopotentials.28 The PBE exchange-correlation functional29 accounted for electron exchange and correlation interactions, and the inclusion of the Grimme D3 correction accounted for dispersion interactions.30 The plane-wave cutoff energy was 500 eV, and the Monkhorst−Pack k-mesh was 4 × 4 × 1 and 4 × 2 × 1 for geometry optimization for the STO/graphene and STO/CNR systems, respectively. Electronic degrees

of freedom have converged to 1 × 10−6 eV. We have extensively tested the electronic smearing parameters to correctly describe the electronic properties of the free graphene (metallic) and CNR (semiconducting) and chose the Methfessel−Paxton method with a width of 0.15 eV for the free graphene and STO/graphene interface and Gaussian smearing with a width of 0.1 eV for the free CNR and STO/CNR interface.

Boltzmann Transport Calculations and Electronic Density of States. The transport properties were calculated using the Boltzmann transport equation as implemented in the BoltzTraP code.31 For this purpose, the Kohn−Sham eigenenergies were calculated on a very dense 24 × 24 × 1 k-point mesh for the free graphene and STO/graphene interface and a 16 × 8 × 1 k-point mesh for the free CNR and STO/CNR interface. These settings were also used to evaluate the electronic density of states (DOS). The transport calculations are performed as a function of temperature and chemical potential employing the constant relaxation time (τ) approximation (CRTA), which neglects the weak energy dependence of τ but recovers some doping and temperature dependence.31 The CRTA methodology has been successfully applied to graphene/CNR32 and oxide thermoelectric materials.33−35 Within this methodology, τ is exactly canceled in the expression of the Seebeck coefficient and thus can be directly evaluated from the first-principles band structure. While the thermopower can be obtained without any adjustable parameters using the CRTA, the evaluation of electronic conductivity σ and the electronic part of the thermal conductivity requires knowledge of τ. Because the first-principles calculations do not give the actual scattering time, we will discuss here only σ*τ−1.

Results and discussion

Structural Parameters of STO/Graphene and STO/ CNR Interfaces.

First, we report the energetic and structural properties of the interfaces. It has been reported that the surface energy of Ti- and Sr-terminated STO surfaces is almost the same,17 and because both could coexist, we investigate adsorption of graphene and CNR on both surface terminations. The atomic structure of the optimized interfaces is shown in Figure 2.

Two key results emerge from the calculations. First, CNRs have an adsorption energy higher than that of graphene and adsorb with a smaller separation from the surface. Second, it is more energetically favorable for both graphene and CNR to adsorb onto the Sr-terminated (001) surface rather than the Ti-terminated (001) surface. A further observation is the structural distortions in the graphene and CNR. The rumpling of the graphene sheet is negligible, with a standard deviation from perfect flatness of 0.036 and 0.004 Å for the Ti- and Sr-terminated STO, respectively. However, for both Ti- and Sr-terminated STO, the CNR edge aligns with the rows of the surface oxygen atoms as shown in panels e and g of Figure 2, resulting in a buckling of the CNR

(Figure 2f,h) by 0.3 and 0.1 Å as measured by the average distance between outermost carbons and hydrogens along the surface normal for the Ti- and Sr-STO surface, respectively. The calculated STO−graphene (CNR) distance as defined by the distance between the graphene carbons (CNR hydrogens) and the surface top oxygen layer and adsorption energy per C atom are 3.116 and 3.227 Å (2.819 and 3.050 Å) and 60.0 and 70.0 meV (91.0 and 124 meV) for the Ti/Sr-STO surface, respectively. All of these structural and energetic features have their origin in the electronic structure, and this is further analyzed in the next section.

Electronic Structure of Interfaces.

Graphene/ TiO2-Terminated STO. Turning to the electronic structure of the Ti-STO/graphene interface, we look first at the electronic density of states (DOS) for the Ti-STO surface, shown in Figure 3. It is readily apparent that the DOSs of the free graphene sheet (Figure 3b) and of STO (Figure 3c) are broadly similar to the DOS of the hybrid and that their interaction is of van der Waals (vdW) character, i.e., no significant modification of the electronic levels of either component. This also suggests that strain has a marginal effect on the DOS of the pure graphene, and this is further supported by the relatively low calculated adsorption energy of the graphene sheet on the Ti-STO surface of 60.0 meV/C atom. Our results therefore show that the weaker TiO2-terminated surface interaction may lead to poor adhesion of graphene. Another feature is that the graphene canonical point (where the valence band touches the conduction band) is preserved upon interaction with Ti-STO (Figure 3b) and aligns with the conduction band minimum (CBM) of STO that is of Ti 3d character (Figure 3a).

Graphene/SrO-Terminated STO. In contrast to Ti-terminated STO, our calculations reveal that the mechanism of interaction of the graphene sheet is radically different for Sr-terminated STO, as shown in Figure 4. In contrast to the good electronic level alignment of graphene on the Ti-STO surface, on Sr-STO the graphene electronic levels align with the valence band maximum (VBM) of the STO surface, which is dominated by the O 2p contribution (Figure 4a). This leads to a stronger interaction of the oxygen with the graphene layer than for the Ti-STO surface. This can also be seen in the modification of the STO DOS below the Fermi level as shown in Figure 4c. This is reflected in the 20−40% higher adsorption energies calculated for the graphene sheet on Sr-STO than on Ti-STO. Although the graphene canonical point is also preserved here, it is now shifted by 0.5 eV below the Fermi level as seen in Figure 4b, which results in an effective n-type doping of the graphene sheet. It needs to be noted that an opposite p-type doping of a graphene sheet on STO has been recently achieved by introduction of STO subsurface oxygen vacancies.22 Described above, the Fermi level shift of graphene can be explained by the difference in the work function between the graphene and substrate that leads to electron transfer between them to equilibrate their Fermi levels.36

CNR/TiO2-Terminated STO. The zigzag CNRs have previously been predicted to have a magnetic ground state with ferromagnetic ordering at each zigzag edge and antiparallel spin orientation at the two edges,18 which agrees with our calculations. Because of edge magnetization, a staggered sublattice potential is introduced on the hexagonal carbon lattice, and a band gap appears (see Figure 5b). The edge states around the Fermi level form flat bands18 that give rise to a very large sharp DOS in the vicinity of the Fermi level as shown in Figure 5b. Moreover, the transport properties of carbon nanoribbons are closely related to their symmetry.37 Figure 5a shows the total and projected onto CNR atoms spin-polarized DOS for the Ti-STO/CNR interface (for the PDOS of Sr, Ti, and O, see Figure 3a and Figure 4a).

As one can see from Figure 5a, the magnetic properties of the CNR are preserved upon interaction with the Ti-STO where two spin channels are intact as in the free CNR (Figure 5b). The comparison between the DOS of the free and adsorbed CNR reveals that its electronic levels are only marginally altered by the presence of the surface (Figure 5b,c), similar to the case discussed above for the Ti-STO/graphene interface. The most interesting aspect of this system is the electronic level alignment between the CNR and STO surface. The CNR highest occupied molecular orbital (HOMO) aligns with the middle of the Ti-STO surface band gap, whereas the lowest unoccupied molecular orbital (LUMO) aligns with its CBM, as highlighted in Figure 5a. Thus, the band gap of the Ti-STO is lowered, but the semiconducting properties of the CNR are preserved. The positioning of the CNR's HOMO charge that is carried in the middle of the STO band gap resembles an n-type doping of STO. Therefore, such hybrid interfaces can provide a new way of decreasing a band gap and simultaneously increasing the carrier concentration of an oxide. The CNR's band gap can be tuned by changing the CNR width and chirality.18,19 For example, it is known that the band gap of semiconducting CNRs decreases with an increase in their width.18 Therefore, the desired modification of the material electronic properties could in principle be achieved by selectively matching the CNR with the desired width/band gap to match the surface electronic properties.

CNR/SrO-Terminated STO. The DOS of the Sr-STO/ CNR surface is shown in Figure 6a–c. Like those of the Sr-STO/graphene interface, the electronic levels of the interface are significantly modified compared to those of the free CNR (Figure 6b) and STO surface (Figure 6c). In contrast to the Ti-STO/CNR interface, the system has a metallic character and the VBM has both STO and CNR character (Figure 6a). The new CNR states appear at the Fermi level as shown in Figure 6b and are a result of hybridization between the electronic levels of the surface O 2pz and π orbitals of the CNR carbons, which results in a covalent bond between the CNR and Sr-STO.

The alignment of the Fermi level that cuts the top VB of the Sr-STO (Figure 6c) suggests the system has p-type character, which is confirmed by the calculated positive Seebeck coefficient as discussed below. Therefore,

here as well as in the STO/graphene interface, the interaction with the different termination of the STO surface leads to a change in the conductivity character, i.e., n-type and p-type for the interface with Ti-STO and Sr-STO interfaces, respectively. These changes in the electronic structure directly affect the calculated Seebeck coefficient and electronic conductivity. In the following section, we discuss the evolution of the Seebeck coefficient and electronic conductivity for these systems as a function of temperature and electronic chemical potential.

Electronic Transport Properties of Graphene/STO and CNR/STO Interfaces.

In solids, both charge and heat flows are simultaneously generated when an electrochemical potential or a temperature gradient is present, resulting in new properties. The Seebeck coefficient and electrical conductivity are determined by the band structure and electron scattering mechanisms. We find that the interaction of the graphene and CNR with the STO alters the electronic properties, the Seebeck coefficient, and the electronic conductivity of the pristine ones. Figure 7 shows the calculated Seebeck coefficient as a function of electronic chemical potential and temperature as well as $\sigma^*\tau-1$ as a function of electronic chemical potential for the free graphene sheet and CNR as well as their interfaces with STO.

The calculated maximum absolute values of the Seebeck coefficient are 185 and 1095 μV/K for the free graphene and CNR, respectively (panels a and d of Figure 7, respectively). The 5-fold increase in the Seebeck coefficient for CNR is a result of its one-dimensional structure, which introduces the sharp DOS peaks around the Fermi level as shown in Figure 6b. This is in qualitative agreement with the tight-binding results of Ouyang and Guo,38 who found that the calculated Seebeck coefficient near the Fermi level was on the order of millivolts per kelvin for semiconducting CNRs but in the range of microvolts per kelvin for graphene. Looking at the evolution of the Seebeck coefficient with temperature, we observe that its absolute value increases for the Ti-STO/graphene interface (Figure 7b) and decreases for the Ti-STO/CNR interface (Figure 7e) as the temperature increases. The latter behaves as the free CNR (Figure 7e), whereas the former behaves in opposite way, decreasing with temperature (Figure 7b). This shows that the Seebeck coefficient and the electronic conductivity of the hybrid material are dominated by the CNR for the Ti-STO/CNR interface but are of a more complex form for the Ti-STO/graphene interface. This is also seen in the calculated $\sigma^*\tau-1$ in Figure 7c, which shows a pronounced asymmetry around the Fermi level for the Ti-STO/graphene interface as compared to that for free graphene (see Figure 7c). This is a result of the electronic level alignment between the graphene and Ti-STO discussed above and is shown in Figure 2a. The graphene Dirac point aligns with the CBM of STO; thus, the DOS (and $\sigma^*\tau-1$) below the Fermi level of the Ti-STO/graphene interface behaves like that from the pristine graphene sheet as its occupied states fill the former band gap of Ti-STO (Figure 7c) but because of the

contribution from the empty states of Ti-STO deviates above the Fermi level. With an increase in temperature and chemical potential, the charge carriers start to populate the CB, the asymmetry of which leads to a different behavior of the transport properties as in the case of the free graphene sheet. The different behavior of the Seebeck coefficient of the adsorbed CNR and graphene sheet, despite the electronic structure being almost identical to that of their free-standing counterparts, may be attributed to the functional properties of STO, such as a high dielectric constant that can modify to a different extent the electronic environment of the CNR and graphene on STO.20−22 The calculated Seebeck coefficient and electronic conductivity are strikingly different for the Sr-STO interface (see panels b and c of Figure 7). The Seebeck coefficient in both cases has a positive value, indicating the change in carrier from electrons to holes. Moreover, because of the electronic states crossing the Fermi level that arise from the interaction between the components, the system has a metallic character. In summary, the interaction of graphene and CNR with a different termination of the STO surface leads not only to the change in the conductivity type from n-type (Ti-STO) to p-type (Sr-STO) but also to a change in the behavior from semiconducting to metallic as in the case of the STO/CNR interface. This may have important consequences for the operation of nanoelectronic devices based on such hybrid materials and guide their design.

Conclusions

In this work, we have studied the structural, electronic, and thermoelectric transport properties of the interfaces of graphene and CNR with SrTiO3 (001). Our results reveal the following key points. (1) Graphene and CNR interact weakly with the TiO2-terminated STO surface (Ti-STO) via van der Waals interactions, leading to little change in the electronic structure. In contrast, both graphene and CNR chemisorb onto the SrO-terminated STO (Sr-STO) surface with higher adsorption energies, leading to significant changes in electronic structure. (2) Carbon nanoribbons have a very high calculated Seebeck coefficient that originates from their one-dimensional structure, which persists upon interaction with the Ti-STO surface. Moreover, such an interaction places CNR's HOMO levels in the middle of the Ti-STO band gap, which resembles n-type doping of the oxide. (3) Interaction of both graphene and carbon nanoribbons with Sr-STO leads to a significant modification of the electronic levels and leads to a p-type electronic conductivity, although the magnitude is much lower than that of the n-type doping at the Ti-STO interface. Our results show that it is possible to control the nature of the electronic conductivity of a hybrid thermoelectric system by optimizing the interface surfaces between different surface terminations.

Author Information

ORCID

Jakub D. Baran: 0000-0003-1582-5083

Christopher Eames: 0000-0002-5548-2655

Marco Molinari: 0000-0001-7144-6075

M. Saiful Islam: 0000-0003-3882-0285

Stephen C. Parker: 0000-0003-3804-0975

Acknowledgments

This work was funded by EPSRC Programme Grants EP/ K016288/1 and EP/I03601X/1. Computations were performed on ARCHER through the Materials Chemistry Consortium funded by EPSRC Grant EP/L000202 and the STFC Hartree Centre (Daresbury Laboratory, Warrington, U.K.) High Performance Computing facilities. Part of this work is funded by "Materials Research by Information Integration" Initiative (MI2I) project of the Support Program for Starting Up Innovation Hub from the Japan Science and Technology Agency (JST).

References

(1) Kovalevsky, A. V.; Yaremchenko, A. A.; Populoh, S.; Thiel, P.; Fagg, D. P.; Weidenkaff, A.; Frade, J. R. Towards a high thermoelectric performance in rare-earth substituted SrTiO3: effects provided by strongly-reducing sintering conditions. Phys. Chem. Chem. Phys. 2014, 16, 26946−26954.

(2) Snyder, G. J.; Toberer, E. S. Complex thermoelectric materials. Nat. Mater. 2008, 7, 105−114.

(3) Biswas, K.; He, J.; Blum, I. D.; Wu, C.-I.; Hogan, T. P.; Seidman, D. N.; Dravid, V. P.; Kanatzidis, M. G. High-performance bulk thermoelectrics with all-scale hierarchical architectures. Nature 2012, 489, 414−418.

(4) Dresselhaus, M. S.; Chen, G.; Tang, M. Y.; Yang, R. G.; Lee, H.; Wang, D. Z.; Ren, Z. F.; Fleurial, J. P.; Gogna, P. New Directions for Low-Dimensional Thermoelectric Materials. Adv. Mater. 2007, 19, 1043−1053.

(5) Wan, C.; Gu, X.; Dang, F.; Itoh, T.; Wang, Y.; Sasaki, H.; Kondo, M.; Koga, K.; Yabuki, K.; Snyder, G. J.; Yang, R.; Koumoto, K. Flexible n-type thermoelectric materials by organic intercalation of layered transition metal dichalcogenide TiS2. Nat. Mater. 2015, 14, 622−627.

(6) Chen, Y.; Jayasekera, T.; Calzolari, A.; Kim, K. W.; Buongiorno Nardelli, M. Thermoelectric properties of graphene nanoribbons, junctions and superlattices. J. Phys.: Condens. Matter 2010, 22, 372202.

(7) Srivastava, D.; Norman, C.; Azough, F.; Schafer, M. C.; Guilmeau, E.; Kepaptsoglou, D.; Ramasse, Q. M.; Nicotra, G.; Freer, R. Tuning the thermoelectric properties of A-site deficient SrTiO3 ceramics by vacancies and

carrier concentration. Phys. Chem. Chem. Phys. 2016, 18, 26475−26486.

(8) Lin, Y.; Norman, C.; Srivastava, D.; Azough, F.; Wang, L.; Robbins, M.; Simpson, K.; Freer, R.; Kinloch, I. A. Thermoelectric Power Generation from Lanthanum Strontium Titanium Oxide at Room Temperature through the Addition of Graphene. ACS Appl. Mater. Interfaces 2015, 7, 15898−15908.

(9) Novoselov, K. S.; Geim, A. K.; Morozov, S. V.; Jiang, D.; Zhang, Y.; Dubonos, S. V.; Grigorieva, I. V.; Firsov, A. A. Electric Field Effect in Atomically Thin Carbon Films. Science 2004, 306, 666−669.

(10) Seol, J. H.; Jo, I.; Moore, A. L.; Lindsay, L.; Aitken, Z. H.; Pettes, M. T.; Li, X.; Yao, Z.; Huang, R.; Broido, D.; Mingo, N.; Ruoff, R. S.; Shi, L. Two-Dimensional Phonon Transport in Supported Graphene.
Science 2010, 328, 213−216.

(11) Zuev, Y. M.; Chang, W.; Kim, P. Thermoelectric and Magnetothermoelectric Transport Measurements of Graphene. Phys. Rev. Lett. 2009, 102, 096807.

(12) Balandin, A. A. Thermal properties of graphene and nanostructured carbon materials. Nat. Mater. 2011, 10, 569−581.

(13) Balandin, A. A.; Ghosh, S.; Bao, W.; Calizo, I.; Teweldebrhan, D.; Miao, F.; Lau, C. N. Superior Thermal Conductivity of Single-Layer Graphene. Nano Lett. 2008, 8, 902−907.

(14) Dorgan, V. E.; Behnam, A.; Conley, H. J.; Bolotin, K. I.; Pop, E. High-Field Electrical and Thermal Transport in Suspended Graphene. Nano Lett. 2013, 13, 4581−4586.

(15) Kim, J. Y.; Grossman, J. C. High-Efficiency Thermoelectrics with Functionalized Graphene. Nano Lett. 2015, 15, 2830−2835.

(16) Chen, X.-K.; Xie, Z.-X.; Zhou, W.-X.; Tang, L.-M.; Chen, K.-Q. Phonon wave interference in graphene and boron nitride superlattice. Appl. Phys. Lett. 2016, 109, 023101.

(17) Yeandel, S. R.; Molinari, M.; Parker, S. C. Nanostructuring perovskite oxides: the impact of SrTiO3 nanocube 3D self-assembly on thermal conductivity. RSC Adv. 2016, 6, 114069−114077.

(18) Son, Y.-W.; Cohen, M. L.; Louie, S. G. Energy Gaps in Graphene Nanoribbons. Phys. Rev. Lett. 2006, 97, 216803.

(19) Barone, V.; Hod, O.; Scuseria, G. E. Electronic Structure and Stability of Semiconducting Graphene Nanoribbons. Nano Lett. 2006, 6, 2748−2754.

(20) Couto, N. J. G.; Sacepé,B.; Morpurgo, A. F. Transport through Graphene on SrTiO3. Phys. Rev. Lett. 2011, 107, 225501.

(21) Park, J.; Kang, H.; Kang, K. T.; Yun, Y.; Lee, Y. H.; Choi, W. S.; Suh, D. Voltage Scaling of Graphene Device on SrTiO3 Epitaxial Thin Film. Nano Lett. 2016, 16, 1754−1759.

(22) Kang, K. T.; Kang, H.; Park, J.; Suh, D.; Choi, W. S. Quantum Conductance Probing of Oxygen Vacancies in SrTiO3 Epitaxial Thin Film using Graphene. Adv. Mater. 2017, 29, 1700071.

(23) Gogoi, P. K.; Trevisanutto, P. E.; Yang, M.; Santoso, I.; Asmara, T. C.; Terentjevs, A.; Della Sala, F.; Breese, M. B. H.; Venkatesan, T.; Feng, Y. P.; Loh, K. P.; Neto, A. H. C.; Rusydi, A. Optical conductivity renormalization of graphene on SrTiO3 due to resonant excitonic effects mediated by Ti-3d orbitals. Phys. Rev. B: Condens. Matter Mater. Phys. 2015, 91, 035424.

(24) Eglitis, R. I.; Vanderbilt, D. First-principles calculations of atomic and electronic structure of SrTiO3 (001) and (011) surfaces. Phys. Rev. B: Condens. Matter Mater. Phys. 2008, 77, 195408.

(25) Kresse, G.; Hafner, J. Ab initio molecular dynamics for liquid metals. Phys. Rev. B: Condens. Matter Mater. Phys. 1993, 47, 558−561.

(26) Kresse, G.; Hafner, J. Ab initio molecular-dynamics simulation of the liquid-metal–amorphous-semiconductor transition in germa-nium. Phys. Rev. B: Condens. Matter Mater. Phys. 1994, 49, 14251− 14269.

(27) Kresse, G.; Furthmüller, J. Efficiency of ab-initio total energy calculations for metals and semiconductors using a plane-wave basis set. Comput. Mater. Sci. 1996, 6, 15−50.

(28) Blöchl, P. E. Projector augmented-wave method. Phys. Rev. B: Condens. Matter Mater. Phys. 1994, 50, 17953−17979.

(29) Perdew, J. P.; Burke, K.; Ernzerhof, M. Generalized Gradient Approximation Made Simple. Phys. Rev. Lett. 1996, 77, 3865−3868.

(30) Grimme, S. Semiempirical GGA-type density functional constructed with a long-range dispersion correction. J. Comput. Chem. 2006, 27, 1787−1799.

(31) Madsen, G. K. H.; Singh, D. J. BoltzTraP. A code for calculating band-structure dependent quantities. Comput. Phys. Commun. 2006, 175, 67−71.

(32) Muley, S. V.; Ravindra, N. M. Thermoelectric Properties of Pristine and Doped Graphene Nanosheets and Graphene Nanorib-bons: Part I. JOM 2016, 68, 1653−1659.

(33) Molinari, M.; Tompsett, D. A.; Parker, S. C.; Azough, F.; Freer, R. Structural, electronic and thermoelectric behaviour of CaMnO3 and CaMnO(3-δ). J. Mater. Chem. A 2014, 2, 14109−14117.

(34) Baran, J. D.; Molinari, M.; Kulwongwit, N.; Azough, F.; Freer, R.; Kepaptsoglou, D.; Ramasse, Q. M.; Parker, S. C. Tuning Thermoelectric Properties of Misfit Layered Cobaltites by Chemically Induced Strain. J. Phys. Chem. C 2015, 119, 21818−21827.

(35) Baran, J. D.; Kepaptsoglou, D.; Molinari, M.; Kulwongwit, N.; Azough, F.; Freer, R.; Ramasse, Q. M.; Parker, S. C. Role of Structure and Defect Chemistry in High-Performance Thermoelectric Bismuth Strontium

Cobalt Oxides. Chem. Mater. 2016, 28, 7470−7478.

(36) Giovannetti, G.; Khomyakov, P. A.; Brocks, G.; Karpan, V. M.; van den Brink, J.; Kelly, P. J. Doping Graphene with Metal Contacts. Phys. Rev. Lett. 2008, 101, 026803.

(37) Li, Z.; Qian, H.; Wu, J.; Gu, B.-L.; Duan, W. Role of Symmetry in the Transport Properties of Graphene Nanoribbons under Bias.

Phys. Rev. Lett. 2008, 100, 206802.

(38) Ouyang, Y.; Guo, J. A theoretical study on thermoelectric properties of graphene nanoribbons. Appl. Phys. Lett. 2009, 94, 263107.

Figures

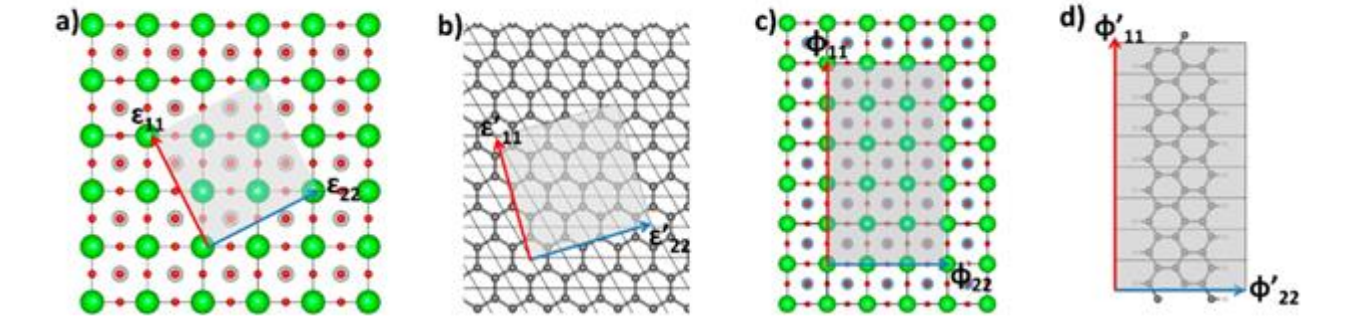

Figure 1. Lattice vectors of (a) STO and (b) graphene sheets in the x−y plane that were matched to create the STO/graphene interface. Similarly, lattice vectors of (c) STO and (d) CNR were matched to create the STO/CNR interface. Color code: dark gray, C; blue, Ti; green, Sr; red, O; white, H. Solid black lines indicate lattice vectors of the primitive unit cell.

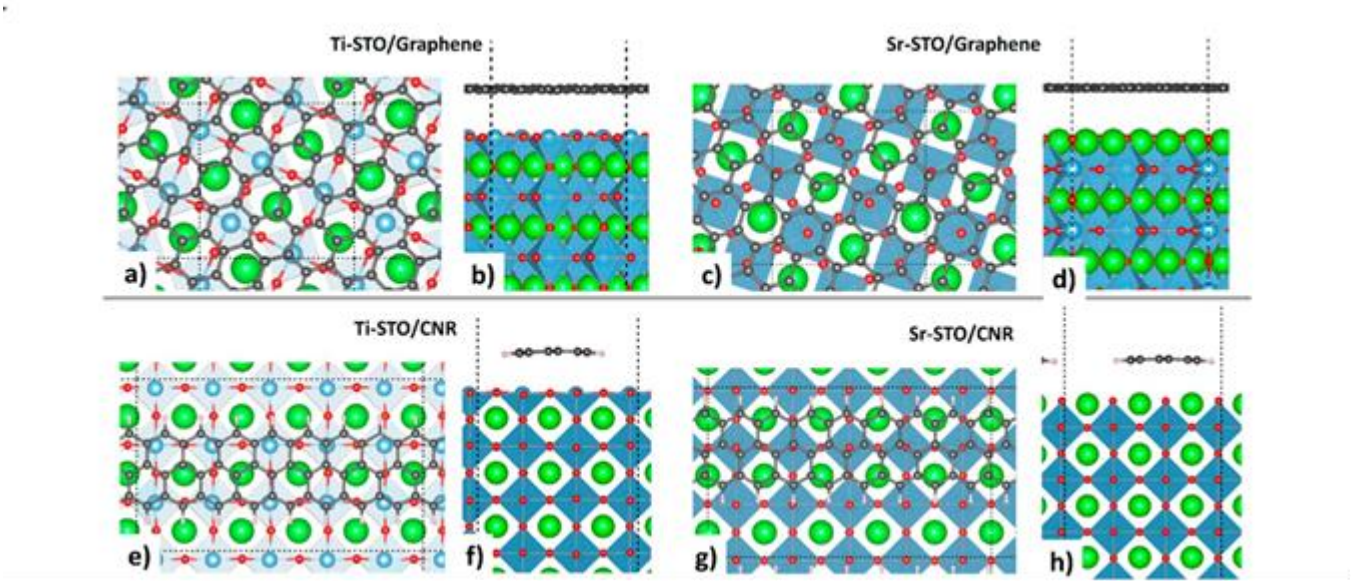

Figure 2. Atomic structure of interfaces between graphene or carbon nanoribbons and the SrTiO3 (001) surface viewed from above and the side: (a and b) graphene on the Ti-terminated surface, (c and d) graphene on the Sr-terminated surface, (e and f) CNR on the Ti-terminated surface, and (g and h) CNR on the Sr-terminated surface. Color code: dark gray, C; blue, Ti; green, Sr; red, O; white, H.

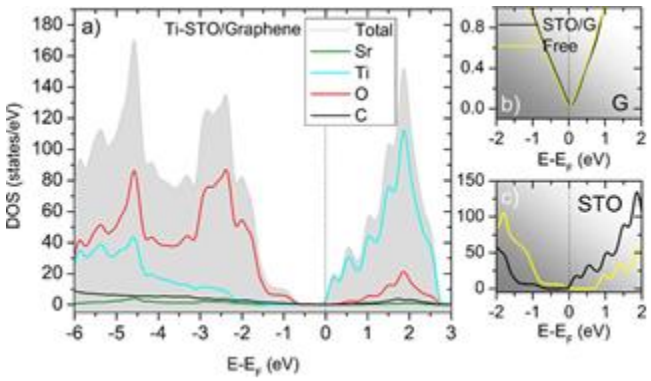

Figure 3. (a) Total and atom-projected DOS for the Ti-STO/ graphene interface. (b) DOS near the Fermi level of graphene and the Ti-STO/graphene interface. (c) DOS near the Fermi level of the clean Ti-STO surface and the Ti-STO/graphene interface. For all the systems, the Fermi level is set at 0 eV, the position of the valence band maximum.

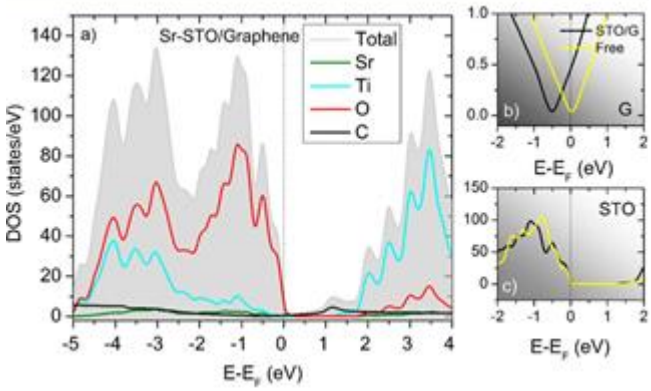

Figure 4. (a) Total and species-projected DOS for the Sr-STO/ graphene interface. (b) DOS near the Fermi level of graphene and the Sr-STO/graphene interface. (c) DOS near the Fermi level of the clean Sr-STO surface and the Sr-STO/graphene interface. For all the systems, the Fermi level is set at 0 eV, the position of the valence band minimum.

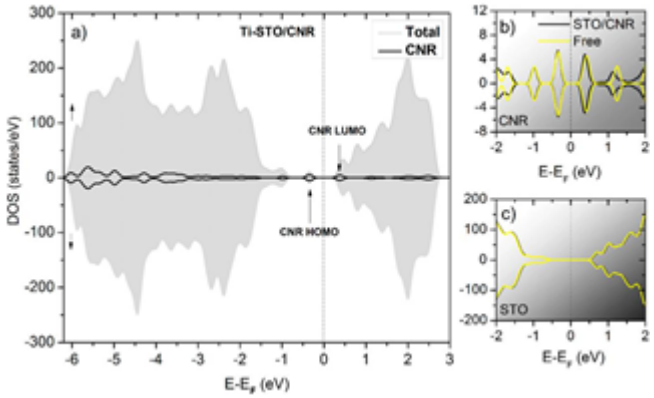

Figure 5. (a) Total DOS and DOS projected onto the CNR atoms of the Ti-STO/CNR interface. (b) DOS of the free and Ti-STO surface interface. (c) DOS near the Fermi level of the clean Ti-STO surface and from the Ti-STO/CNR interface. Positions of the CNR HOMO and LUMO are highlighted. The Fermi level is set up in the middle of the band gap.

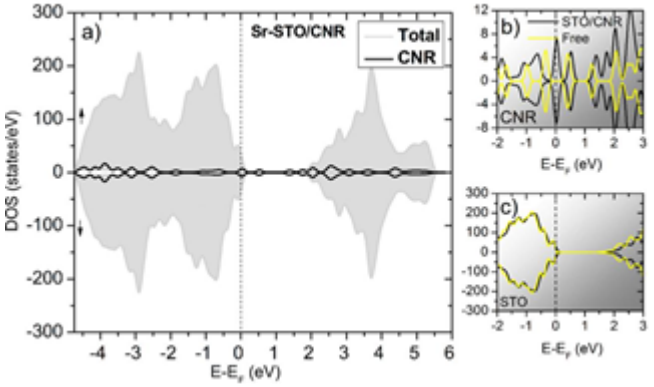

Figure 6. (a) Total DOS of the Sr-STO/CNR interface projected onto CNR atoms. (b) DOS of the free form and the Sr-STO/CNR interface. (c) DOS near the Fermi level of the clean Sr-STO surface and from the Sr-STO/CNR interface. The Fermi level is set up at VBM.

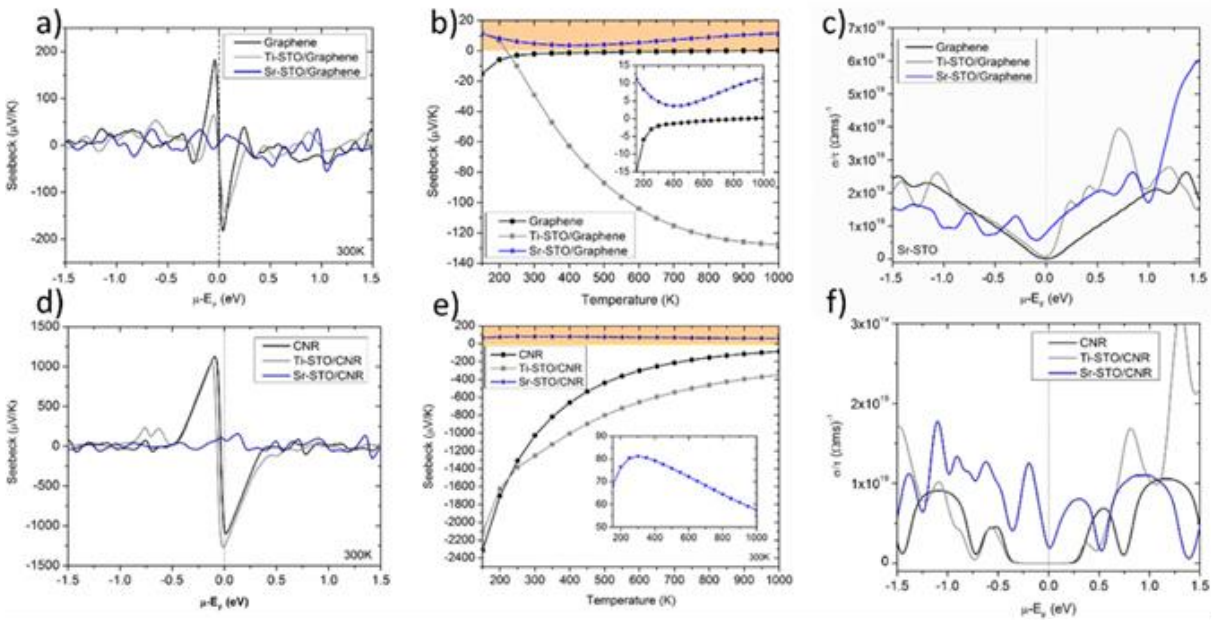

Figure 7. Calculated Seebeck coefficient as a function of (a) chemical potential and (b) temperature for the free graphene and Ti(Sr)-STO/ graphene interface. Calculated Seebeck coefficient as a function of (d) chemical potential and (e) temperature for the free CNR and Ti(Sr)-STO/ CNR interface. Calculated $\sigma^*\tau-1$ as a function of chemical potential for (c) free graphene and the Ti(Sr)-STO/graphene interface and (f) free CNR and the Ti(Sr)-STO/CNR interface. Highlights and insets in panels b and e show regions where the Seebeck coefficient takes a positive value.